






Enabling three-dimensional real-space analysis of ionic colloidal crystallization

Received: 29 August 2023

Accepted: 8 May 2024

Published online: 03 June 2024

 Check for updates

Shihao Zang ¹, Adam W. Hauser ^{1,2}, Sanjib Paul ¹, Glen M. Hocky ^{1,3}  & Stefano Sacanna ¹ 


Structures of molecular crystals are identified using scattering techniques because we cannot see inside them. Micrometre-sized colloidal particles enable the real-time observation of crystallization with optical microscopy, but in practice this is still hampered by a lack of ‘X-ray vision’. Here we introduce a system of index-matched fluorescently labelled colloidal particles and demonstrate the robust formation of ionic crystals in aqueous solution, with structures that can be controlled by size ratio and salt concentration. Full three-dimensional coordinates of particles are distinguished through in situ confocal microscopy, and the crystal structures are identified via comparison of their simulated scattering pattern with known atomic arrangements. Finally, we leverage our ability to look inside colloidal crystals to observe the motion of defects and crystal melting in time and space and to reveal the origin of crystal twinning. Using this platform, the path to real-time analysis of ionic colloidal crystallization is now ‘crystal clear’.

Commonly, crystals are envisioned as perfect structures that are composed of a simple unit cell repeating infinitely in all directions. In reality, however, crystals are of finite size and can exhibit myriad morphologies, as seen, for example, in the appearance of snowflakes¹. Real crystals also contain a number of types of defect, which include vacancies, inclusions or stacking faults, and certain crystal symmetries allow multiple crystals to interpenetrate into ‘twinned’ structures. Micrometre-sized colloidal particles enable us to mimic the behaviour of atomic or molecular systems at a scale where the properties of the system can be probed at a per-particle level using optical microscopy². However, for the most part, we have been limited to inferring the behaviour of these systems by studying them from the outside.

To image colloidal crystals in three dimensions, confocal microscopy is used with fluorescently labelled particles. With this process, a substantial challenge originates from the scattering of laser light off the colloidal particles, where the amount of scattering is directly proportional to the difference in refractive index between the particles and the surrounding medium. To mitigate this issue, previous research has either adjusted the surrounding medium using organic solvents with refractive index values matched to the colloidal polymers or via

engineering colloids from polymers with refractive index values closer to those of the preferred solvent^{3–7}. The use of these three-dimensional (3D) colloidal model systems has been instrumental in pioneering research into phenomena that are not directly observable at the atomic scale, including the nucleation and dynamics of dislocations^{8,9} and the influence of impurities on crystal growth¹⁰. However, the research conducted thus far has been limited to single-component, close-packed crystals. There is a notable gap in the study of crystals that are of adequate size and complexity, where 3D confocal imaging could reveal new insights into the detailed internal structure and dynamics of real crystalline materials.

In a recent study, we reported the polymer-attenuated Coulombic self-assembly (PACS) method, which is a general technique for assembling multi-component colloidal crystals in water by taking advantage of the native surface charge of the colloids^{2,11}. The advantages of the PACS method are that we can form macroscopic colloidal crystals, the methodology is insensitive to the type of building block, and crystals can be fixed for imaging with electron microscopy. These binary crystals are sufficiently complex that they exhibit a range of non-trivial structures, including polymorphism, complex morphologies and

¹Department of Chemistry, New York University, New York, NY, USA. ²Department of Physics, New York University, New York, NY, USA. ³Simons Center for Computational Physical Chemistry, New York University, New York, NY, USA.  e-mail: hockyg@nyu.edu; s.sacanna@nyu.edu

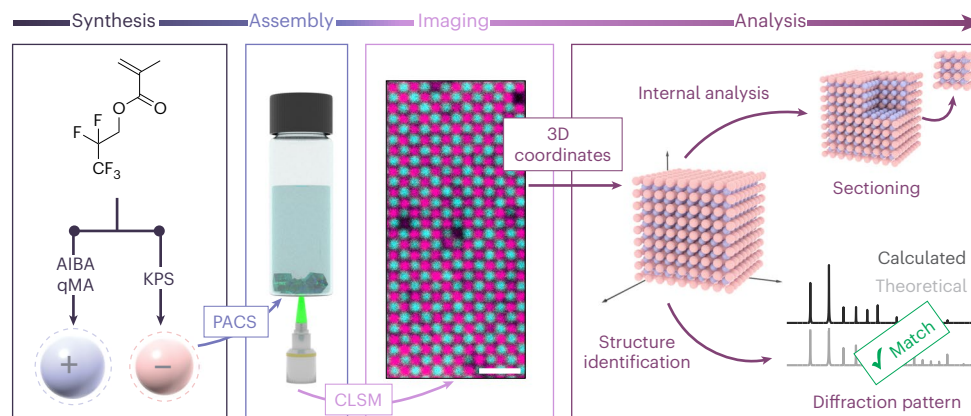


Fig. 1 | Overall strategy. Left to right: particles of low refractive index are synthesized via surfactant-free emulsion polymerization using either KPS or AIBA initiator, then assembled in aqueous solution with salt via PACS. Whereas polystyrene crystals scatter light, PFPMA crystals are nearly transparent in water

and enable us to clearly identify fluorescently labelled positive and negative particles at any given depth. 3D coordinates are reconstructed from z scans, which enable us to inspect the internal structure of the crystals and identify them through scattering analysis. Scale bar, 2 μm .

intricate twinning patterns. Because we can reproducibly create a large variety of binary crystals using the PACS methodology, we hypothesized that we could observe these phenomena at the single-particle level, if we could design a system of index-matched colloids of opposite charge and tunable size ratio.

Here we present a robust platform for generating and internally analysing binary ionic colloidal crystals in aqueous solution with single-particle precision (Fig. 1). We first develop a synthetic protocol for generating colloids of stable positive and negative charge using fluorinated monomers, such that the resulting particles are monodisperse, of tunable size and, crucially, nearly index-matched with water. We then assemble these particles into crystals whose structure and assembly processes can be tuned by changing the size ratio and salt concentration using the PACS methodology¹¹. For sufficiently large colloidal diameters, typically 450 nm or larger, we are able to distinguish all of the particles within a binary ionic crystal, and reconstruct the full internal 3D structure up to depths of ~200 layers. Using the extracted 3D coordinates, we are able to identify the resulting crystal structure through internal analysis (Supplementary Video 1) and via comparison of the generated scattering patterns with reference crystal structures. The ability to see inside these crystals gives unique insight into phenomena previously only observed from without, such as the structure and density of different types of defect and the origin of crystal twinning. Moreover, our ability to scan and reconstruct crystals *in situ* enables us to observe dynamic phenomena such as rearrangement within defects and the melting of crystals, which is not possible via more invasive procedures that are commonly used to look inside crystalline assemblies (Supplementary Video 2).

Synthesis of optically transparent colloids with opposite charges

We first developed a synthetic approach to produce charged monodisperse building blocks from low-refractive-index fluorinated polymers, as described in the Methods and Extended Data Fig. 1. Using potassium persulfate (KPS) as an initiator, monodisperse pentafluoropropyl methacrylate (PFPMA) particles could be formed and retained a negative surface charge indefinitely. To obtain similar quality colloids with a stable positive charge, we used the 2,2'-azobis(2-methylpropionamide) dihydrochloride (AIBA) initiator with a small amount of (2-(methacryloyloxy)ethyl)trimethylammonium chloride (qMA) comonomer. The diameter of the colloid particles could be tuned smoothly in the range of 140–400 nm by changing the ratio of monomer to comonomer; monodisperse particles used in this study with a diameter larger than

400 nm were formed via seeded growth using smaller particles. To enable assembly via PACS, all particles were coated in Pluronic F108 poloxamer, resulting in a polymer brush of length approximately 10 nm (ref. 12). Particles were fluorescently labelled in two colours by swelling and deswelling the particles using THF in the presence of BODIPY dyes of different wavelengths¹³.

Assembly and depth profiling

Oppositely charged colloids of either polystyrene (PS) or PFPMA rapidly assembled into colloidal crystals under optimal concentrations of dissolved NaCl, as described in the Methods. Figure 2a shows faceted crystals formed from either PS or PFPMA using a size ratio of ~1.14 of positive to negative particles, which we have previously shown produces crystals that are isostructural to CsCl. Those from PS (refractive index $n = 1.6$) are opaque when observed using a bright-field microscope, whereas those from PFPMA ($n = 1.39$) are translucent in water. When 40% dimethyl sulfoxide (DMSO) is introduced, the refractive index values of the solution and PFPMA are matched (Extended Data Fig. 2a,b) and the particles are completely transparent; however, the presence of faceted crystals is clear when using fluorescence imaging.

In many cases, the assembly of crystals is templated by the surface due to the attraction of positive particles to the inherent negative charge of the glass substrate; this results in one crystal plane being parallel to the surface, and thus imaging at different depths corresponds to imaging individual layers of particles. In Fig. 2b,c, we show the received fluorescence intensity at different depths relative to the intensity at 1 μm ; for PS, the intensity decays rapidly, losing >90% over just ~7 μm , whereas for PFPMA, ~90% of the intensity is not lost until ~60 μm in pure water or ~70 μm in the water/DMSO mixture (we note that, given the size of the particles and the structure of this crystal, 5 μm corresponds to more than ten unit cells deep into the crystal). At the same time, we observe that the fluorescence emitted by individual particles located on the same horizontal plane can be distinctly differentiated. Finally, Fig. 2d shows the fluorescence images obtained from our PS crystal in water and the PFPMA crystal in water at the same depth of 5 μm , and Extended Data Fig. 2c,d shows the confocal slices ranging from 1 to 90 μm for PS and PFPMA in water/DMSO. Both correspond to the (100) plane of CsCl, as described in the next section, but this is only barely discernible in the case of PS, whereas it is quite evident for our index-matched system. We attribute the eventual loss of the fluorescence intensity at ~70–80 μm to bleaching, due to the scanning of all layers until that depth, and hence greater depths can also be accessed if we only want to peer into the bulk.

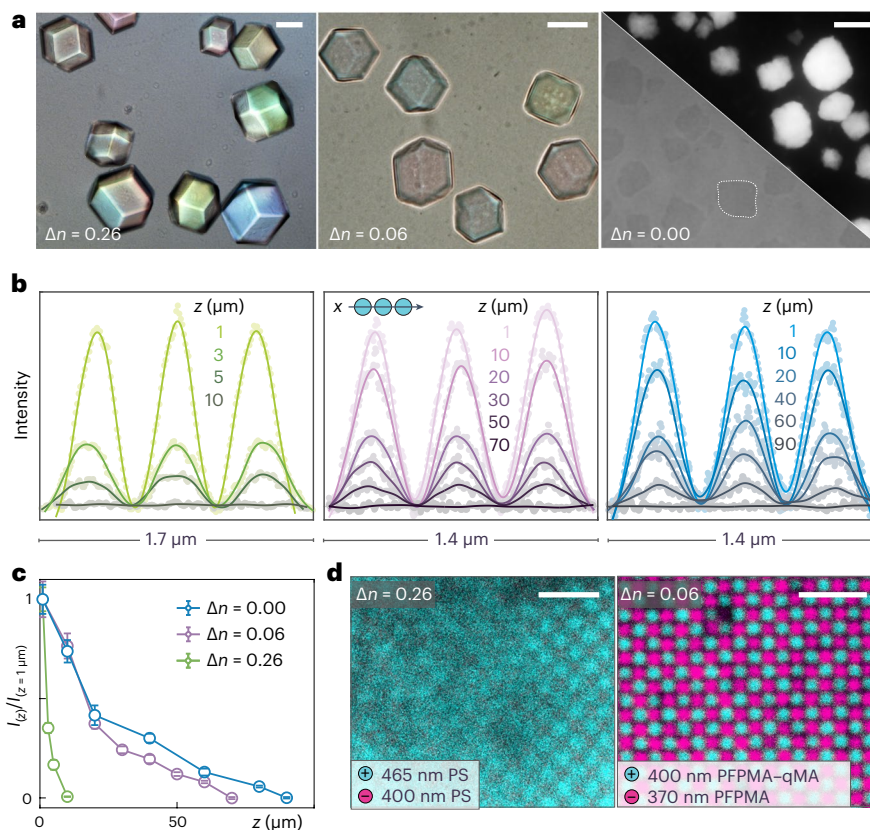


Fig. 2 | Assembly and imaging of binary crystals. **a**, Binary crystals are assembled from oppositely charged particles with a positive to negative size ratio of 1.14. Those with PS particles are opaque in water (left), whereas those assembled from PFPMA are translucent (middle). PFPMA crystals in 40% DMSO (right) are optically transparent (left side) but visible through fluorescence imaging (right side); in the optical microscope image, one of the crystals is outlined by the dotted line. Scale bars, 25 μm . Δn , difference in refractive index between the colloidal crystals and the medium. **b**, Fluorescence intensity line scans at different depth (z) values. Individual particle positions are clearly

identifiable at small depths but cannot be resolved deeper than 5 μm for PS (left), whereas the positions can be resolved at tenfold greater depths using PFPMA in water (middle) or 40% DMSO (right). The solid lines are the fits to a sum of three Gaussians. **c**, Average intensity (I) difference between the peaks and valleys of the line profiles at different z values normalized by that at $z = 1 \mu\text{m}$ for each system. Data are shown as the mean \pm s.d. with a sample size of nine at each z . **d**, Fluorescence images in the x - y plane taken at a depth $z = 5 \mu\text{m}$ for PS crystals (left) and PFPMA crystals (right) in water. Scale bars, 2 μm .

3D reconstruction and crystal identification

The ability to pinpoint the 3D location of individual particles without drying the samples enables us to study the internal structure of these colloidal crystals in situ. First, we reconstruct the 3D positions of the particles from the crystals shown previously in Fig. 2. Here, we used data from scans up to 20 μm obtained via confocal laser scanning microscopy (CLSM) to reconstruct the positions of positive and negative particles separately using the Trackpy package¹⁴, via the method of Crocker and Grier¹⁵. Figure 3a shows rectangular prismatic chunks of the reconstructed crystals, rendered using Blender software¹⁶. Given our previous work with PACS, we predicted that the structures formed with a size ratio in the range of 0.74–1.00 will adopt CsCl-type structures¹¹. Using the reconstructed crystal, we were able to find the expected crystal planes for this structure, confirming this hypothesis. Supplementary Video 1 provides a detailed walkthrough, showing the transition from confocal z scans to reconstructed models and, ultimately, to the characteristic crystal planes.

To demonstrate the effectiveness of our approach, we hoped to identify and analyse a colloidal crystal structure not previously observed with PACS. By scanning for particle size and number ratios, we observed large crystals with cubic habits. These were found at a size ratio of 0.78 and a number ratio of 3:1, and consisted of 375 nm positive particles and 480 nm negative particles. Reconstructing this crystal, we were able to clearly identify planes as shown in Fig. 3b, which led us to identify this as being isostructural to Cu_3Au .

Molecular dynamics simulations using our previously developed model¹¹ with parameters taken from these experiments, including a reduced dielectric constant to take into account the presence of DMSO (Methods), show stable crystals with rhombic dodecahedral and cubic habits using the same particle sizes as in the experiment (Extended Data Fig. 3). The agreement between our PFPMA, PS and simulation systems confirms the generality of the PACS approach and the applicability of our simulation model, and supports the adoption of our PFPMA system as a model to study binary ionic crystals more generally.

Having access to all particle positions gives us an alternative means of confirming our crystal structure identification through a more direct comparison with known binary crystal structures. Here we generated simulated X-ray diffraction patterns using Mercury software¹⁷ from the reconstructed coordinates. To do so, we test a hypothesized binary crystal structure such as CsCl, align our reconstructed coordinates to be commensurate with the unit-cell vectors of that lattice and then compute the resulting scattering intensity (Extended Data Fig. 4). Comparison of these intensities with atomic scattering shows excellent agreement between our experimental and molecular dynamics simulation data for both CsCl and Cu_3Au structures (Fig. 3c,d). Collapsed unit cells for the molecular dynamics data show the amount of noise that may be expected for an ideal crystal solely from thermal fluctuations at room temperature, showing that the noise in our reconstructed crystal unit cells also includes noise from particle tracking and probably some amount of structural disorder.

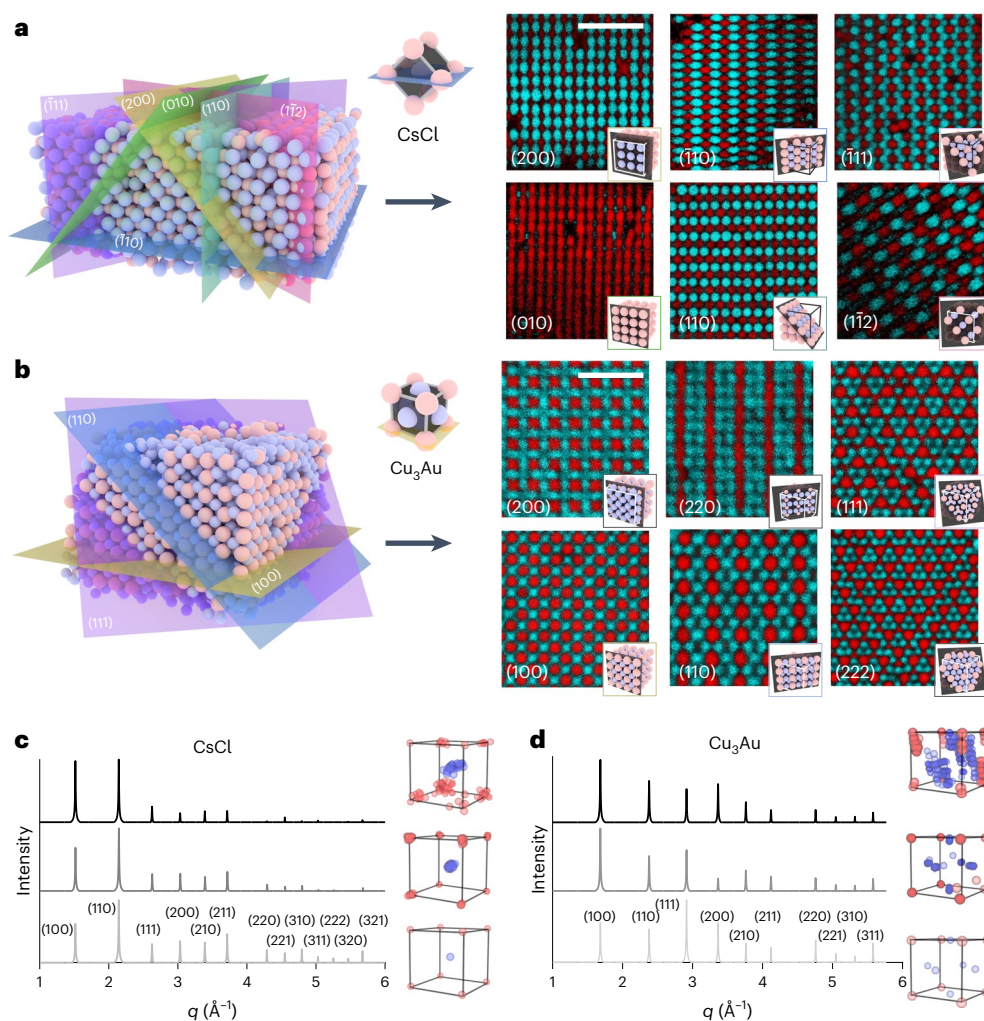


Fig. 3 | 3D crystal reconstruction and structure identification.

a, b, Left: 3D renderings of the reconstructed specimens isostructural to CsCl (**a**) and Cu_3Au (**b**), with slices along various crystallographic planes labelled with the identified Miller indices. Right: corresponding raw CLSM data from those slices, with the insets detailing the anticipated patterns. Scale bars, 2 μm . **c, d,** Generated X-ray diffraction patterns from the coordinates of the

experiment (top), simulation (middle) and theoretical (bottom) body-centred cubic CsCl (**c**) and face-centred cubic Cu_3Au (**d**) crystals. The insets show 50 unit cells superimposed for each dataset to give a sense of the positional variance in the experimental and simulated data. q , length of the reciprocal lattice vector.

Although this procedure requires assuming a unit cell, it is robust enough to reject incorrect guesses. For example, in Extended Data Fig. 4, we show that the scattering pattern that arises from the same data, when assumed to have an α -IrV or a CuAu structure (both of which are distorted CsCl lattices), results in clear disagreement.

Internal crystalline disorder

With our ability to clearly identify all particle positions in hundreds of crystalline layers, we can examine what lies within our colloidal crystals in fine detail. Although the crystals we have generated through PACS form readily and robustly, each contains within them a variety of rare but easily noticed point defects. In Fig. 4a, b, we present the variety of point defects identified after analysing numerous samples, which together comprise thousands of crystal planes. The most basic point defect is a vacancy, which is characterized by the absence of either a positively or negatively charged particle from its standard lattice position. In addition to simple vacancies, we also observe two other prominent defect types. First, there are substitutional defects, where a foreign particle replaces a native particle in the lattice. Second, we note the presence of antisite defects, wherein a positive particle occupies a site intended for a negative particle, and vice versa.

An initial quantification of point defects (in both simulations and experiments) shows that only about 0.1% of the particle positions contain a defect. These crystals were grown on substrates, and there may be some effect of distance from the substrate on the likelihood of finding a defect, although a detailed study of this effect, as well as the effect of changing conditions such as the growth rate, will require additional investigation.

To assess the mobility of internal defects, we performed dynamic studies by tracking the vacancies deep within a CsCl crystal. As demonstrated in Fig. 4c, isolated vacancies remain stationary, even when the crystal is brought to its melting point by allowing the gradual evaporation of solvent, thereby increasing the salt concentration and decreasing the pair potential. This may be due to the densely packed crystalline arrangement resulting in the fluctuation of particle positions that are small compared with the lattice vector. By contrast, the presence of vacancy clusters facilitates particle mobility, even below the crystal's melting point. This behaviour is captured in Extended Data Fig. 5 and Supplementary Video 2, showcasing our ability to map and track particle dynamics in three dimensions, including the internal rearrangement of larger defects, within a CsCl crystal.

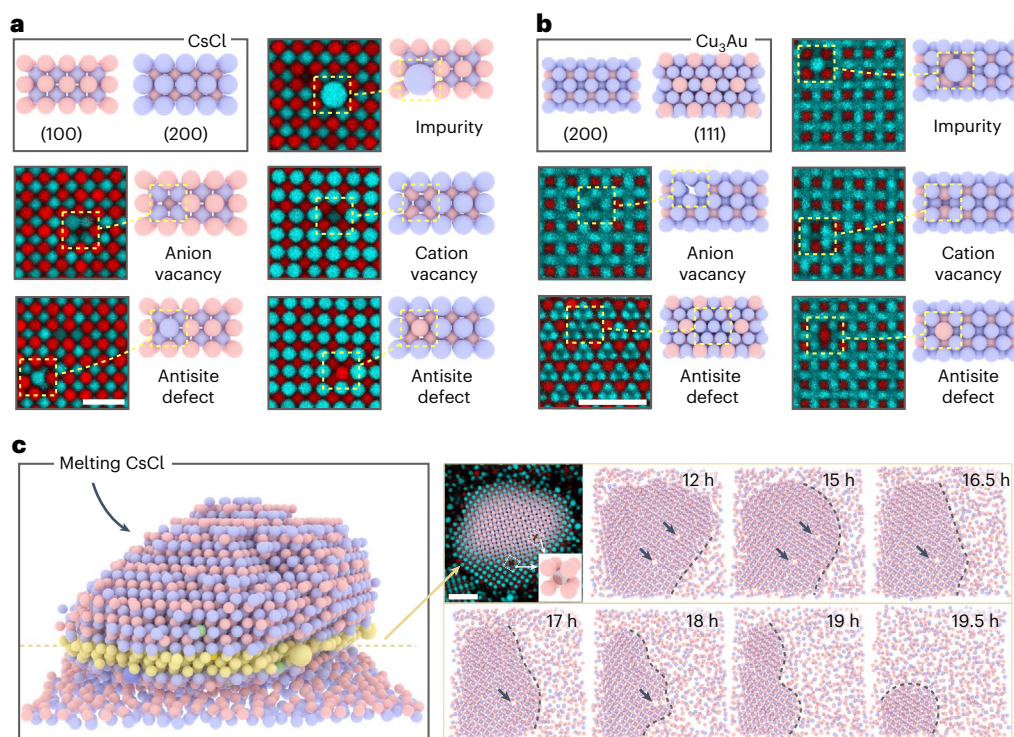


Fig. 4 | Single point defects. **a, b**, Confocal imaging and 3D renderings of the most commonly observed point defects in CsCl-like (**a**) and Cu_3Au -like (**b**) crystals. The 3D renderings in the grey boxes show ideal, defect-free planes. Scale bars, 2 μm . **c**, The left image shows a 3D-reconstructed snapshot of a CsCl crystal imaged while melting due to increased salt concentration resulting from gradual solvent evaporation. As the crystal melts, a 20 h time-lapse of the yellow

cross-section is recorded, showing that isolated vacancies (indicated by the grey arrows in the series on the right) remain stationary. The time-lapse images are rendered reconstructions from real-data particle coordinates extracted from confocal z scans. The first image of the time-lapse series displays the reconstructed image overlaid on the real data, where the inset shows an expanded version of the isolated vacancies highlighted. Scale bar, 3 μm .

Internal structure of twinned crystals

Crystal twinning arises when the two crystal structures align in specific orientations that allow them to share a common plane. Twin laws are mathematical symmetry operations that transform one crystal segment orientation into the other such that this twinning is possible¹⁸. These operations involve a specific point and a specific direction, along with the angle of rotation or the plane of reflection. Twin laws are often given in terms of Miller indices, which represent the normal to the twin plane for reflection twins or the axis of rotation for rotation twins.

Twinning and the single point defects mentioned previously have crucial roles in influencing the material properties, including the mechanical strength, electrical conductivity and optical characteristics. Specifically within the realm of colloidal self-assembly, our capacity to engineer photonic bandgap materials with optimal performance hinges critically on understanding the behaviour of these internal defects.

Here, we illustrate the utility of our model systems as an efficient analytical tool to investigate the twin laws in colloidal crystals. We do this by concurrently visualizing the 3D particle arrangements within the crystal and resolving the global crystal shape. This direct observation unambiguously unravels the internal intricacies of the crystal structure, elucidating the relationship between the particle interactions and the macroscopic crystal form, including the emergence and impact of defects and twinning.

In our cubic crystal systems—which include CsCl, NaCl and Cu_3Au —the most frequently observed type of twinning corresponds to the $\{111\}$ twin law, as illustrated in Fig. 5. This twin law dictates a reflection across a plane that bisects the diagonal of the unit-cell cube.

Exploration of the internal structure of twinned crystals begins with a comprehensive 3D confocal z stack of a specimen followed by

the reconstruction protocol outlined in the previous section. Once reconstructed, we segment the model to discern the characteristics of the twin planes within the crystal. Finally, we utilize the information on the quantity and types of twin planes to interpret the macroscopic crystal shape as observed in scanning electron microscopy (SEM) images.

Taking the example of the Cu_3Au -like assembly in Fig. 5a, inspection of the x - y planes in this case shows a clear intersection of two different crystal axes, consistent with reflection around a single axis. Looking inside our reconstructed crystal, we can clearly see that the intersection planes are the same (corresponding to a (100) plane); a slice through the reconstruction along the mirror plane shows that both share a (111) plane. Figure 5b shows an example SEM image of a fixed PS crystal that shows the same crystal twinning behaviour; inspection of the crystal facets reveals the same intersection of (100) planes along a (111) plane.

So far, we have only discussed twinned structures formed from the interpenetration of two single crystals; however, multiple twin planes within the same crystal can engender a diverse array of macroscopic habits, as shown in Fig. 6. For Cu_3Au , pairs of adjacent (111) twin planes are often encountered. When these planes are parallel, the crystal retains its orientation following the second twinning event (Fig. 6a). Conversely, if the twin boundaries are non-parallel, an isosceles triangle with a vertex angle of 70.5° emerges (Fig. 6b), potentially leading to the manifestation of five-fold symmetry^{19–21}. Further insights into the internal analysis of crystals with multiple twin planes, as well as examples of crystals with a stacking fault, can be found in Extended Data Fig. 6. With this twin law in hand, we can more effectively interpret the prevalence and relative orientation of interpenetrating cubes in large complex crystals, as illustrated in Fig. 6c–e.

Moving forward, we anticipate that our methodology will shed new light on the precise mechanisms of crystal nucleation and growth

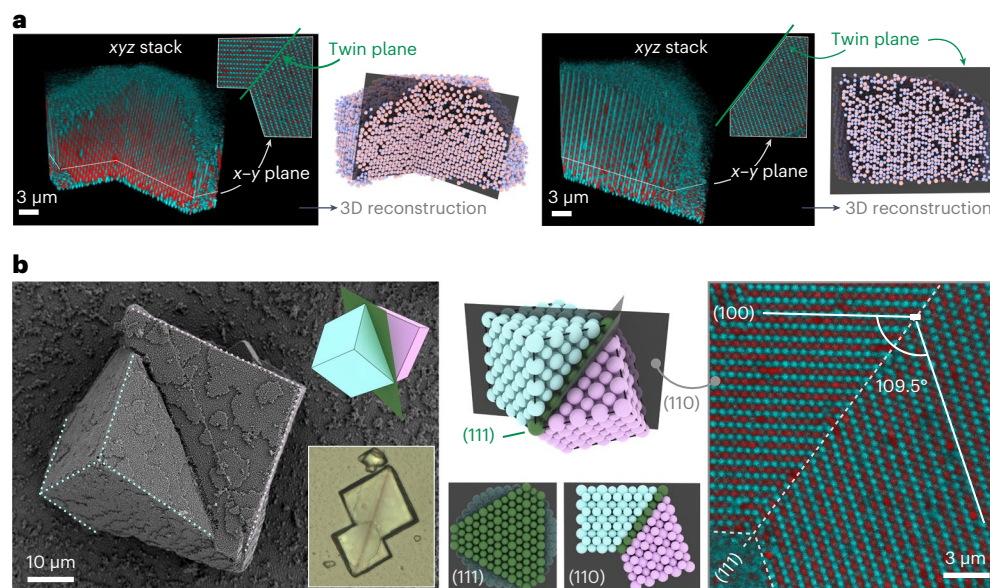


Fig. 5 | Twin boundary analysis in Cu_3Au -like crystals. a, 3D confocal scans and corresponding reconstructions of a crystal (isostructural with Cu_3Au) that exhibits twinning. The twin boundary is characterized as a (111) plane via digital sectioning of the crystal. **b**, The SEM image on the left presents the typical macroscopic habit of a twinned Cu_3Au crystal. The bottom inset provides a lower-resolution bright-field image of a comparable twinned

crystal. The schematics (top inset and middle section) clarify the crystal habit as two interpenetrating cubes connected by a common (111) plane. The confocal scan (right) slices the crystal along the (110) plane, orthogonal to the twin boundary. The intersected (100) planes via the (111) twin plane form an expected 109.5° angle.

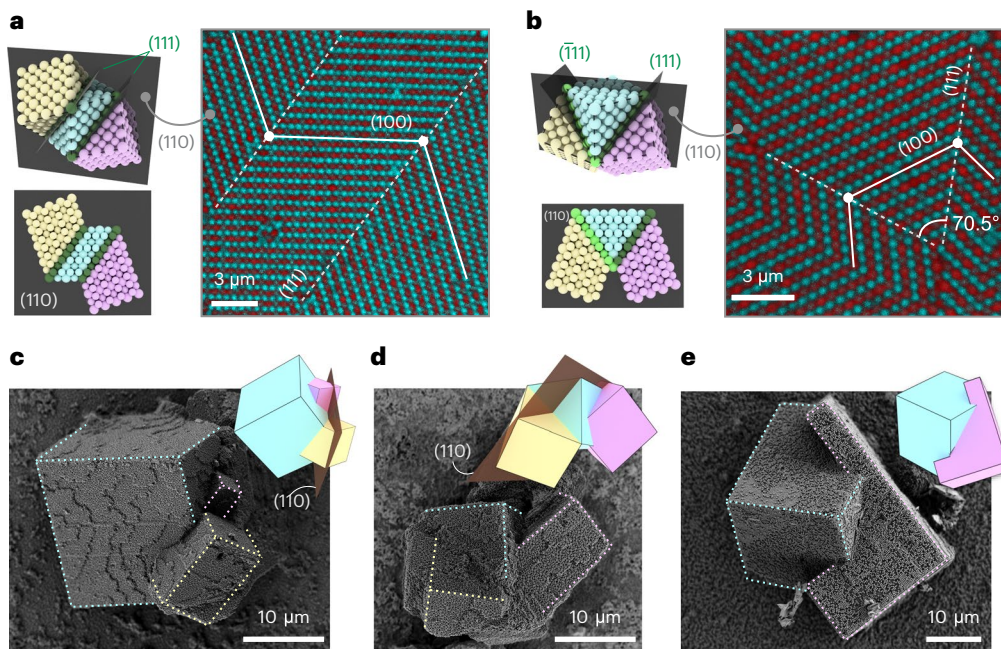


Fig. 6 | Characteristics of double twinning in Cu_3Au -like crystals.

a, b, Schematics (left) and experimental CLSM data (right) illustrate Cu_3Au -like crystals featuring two (111) twin planes. The resultant crystal structure mimics three interlocking cubes sharing a mutual (110) plane and displaying rotational symmetry. If the twin planes are parallel (**a**), the crystal reverts to its original orientation post the second twinning occurrence. Conversely, non-parallel twin planes (**b**) induce a distinct V shape in the crystal. **c, d**, SEM images exhibiting

typical macroscopic shapes for doubly twinned Cu_3Au -like crystals with parallel (**c**) and non-parallel (**d**) (111) twin planes. The insets and corresponding colour-coded dotted lines clarify the orientation of the three interpenetrating crystals. **e**, A similar twinning phenomenon is observed in another cubic structure. This structure, which is isostructural with NaCl, is formed from 300 nm positively charged PS and 130 nm negatively charged PS.

across a broad spectrum of ionic solids and under a diverse range of experimental conditions. Furthermore, by developing fluorinated core-shell building blocks, we expect to greatly increase the precision of particle tracking, especially in densely packed systems. This will not

only catalyse a multitude of fundamental studies that investigate the thermodynamic and kinetic control parameters of crystallization but will also expedite material discovery by enabling the optimization of designer crystal assembly.

Online content

Any methods, additional references, Nature Portfolio reporting summaries, source data, extended data, supplementary information, acknowledgements, peer review information; details of author contributions and competing interests; and statements of data and code availability are available at <https://doi.org/10.1038/s41563-024-01917-w>.

References

1. Libbrecht, K. G. The physics of snow crystals. *Rep. Prog. Phys.* **68**, 855–895 (2005).
2. Hueckel, T., Hocky, G. M. & Sacanna, S. Total synthesis of colloidal matter. *Nat. Rev. Mater.* **6**, 1053–1069 (2021).
3. Leunissen, M. E. et al. Ionic colloidal crystals of oppositely charged particles. *Nature* **437**, 235–240 (2005).
4. van der Wee, E. B. et al. 3D test sample for the calibration and quality control of stimulated emission depletion (STED) and confocal microscopes. *Commun. Biol.* **4**, 909 (2021).
5. Liu, Y. et al. Colloidal organosilica spheres for three-dimensional confocal microscopy. *Langmuir* **35**, 7962–7969 (2019).
6. Kodger, T. E., Guerra, R. E. & Sprakel, J. Precise colloids with tunable interactions for confocal microscopy. *Sci. Rep.* **5**, 14635 (2015).
7. Muluneh, M. Direct visualization of three-dimensional crystallization behavior in microgels. *Phys. Rev. E* **85**, 021405 (2012).
8. Schall, P., Cohen, I., Weitz, D. A. & Spaepen, F. Visualization of dislocation dynamics in colloidal crystals. *Science* **305**, 1944–1948 (2004).
9. Schall, P., Cohen, I., Weitz, D. A. & Spaepen, F. Visualizing dislocation nucleation by indenting colloidal crystals. *Nature* **440**, 319–323 (2006).
10. de Villeneuve, V. W. A. et al. Colloidal hard-sphere crystal growth frustrated by large spherical impurities. *Science* **309**, 1231–1233 (2005).
11. Hueckel, T., Hocky, G. M., Palacci, J. & Sacanna, S. Ionic solids from common colloids. *Nature* **580**, 487–490 (2020).
12. Youssef, M., Morin, A., Aubret, A., Sacanna, S. & Palacci, J. Rapid characterization of neutral polymer brush with a conventional zeta-meter and a variable pinch of salt. *Soft Matter* **16**, 4274–4282 (2020).
13. Kim, A. J., Manoharan, V. N. & Crocker, J. C. Swelling-based method for preparing stable, functionalized polymer colloids. *J. Am. Chem. Soc.* **127**, 1592–1593 (2005).
14. *Trackpy: Fast, Flexible Particle-Tracking Toolkit* (Trackpy Contributors, accessed 1 August 2023); <http://soft-matter.github.io/trackpy/dev/index.html>
15. Crocker, J. C. & Grier, D. G. Methods of digital video microscopy for colloidal studies. *J. Colloid Interface Sci.* **179**, 298–310 (1996).
16. Blender v.4.1 (Blender Foundation, accessed 1 August 2023); <https://www.blender.org/>
17. Macrae, C. F. et al. Mercury 4.0: from visualization to analysis, design and prediction. *J. Appl. Crystallogr.* **53**, 226–235 (2020).
18. Klein, C. & Dutrow, B. *Manual of Mineral Science* 23rd edn (Wiley, 2007).
19. Du, J. S., Zhou, W., Rupich, S. M. & Mirkin, C. A. Twin pathways: discerning the origins of multiply twinned colloidal nanoparticles. *Angew. Chem. Int. Ed.* **60**, 6858–6863 (2021).
20. Song, M. et al. Oriented attachment induces fivefold twins by forming and decomposing high-energy grain boundaries. *Science* **367**, 40–45 (2020).
21. Lee, S. & Glotzer, S. C. Entropically engineered formation of fivefold and icosahedral twinned clusters of colloidal shapes. *Nat. Commun.* **13**, 7362 (2022).

Publisher's note Springer Nature remains neutral with regard to jurisdictional claims in published maps and institutional affiliations.

Springer Nature or its licensor (e.g. a society or other partner) holds exclusive rights to this article under a publishing agreement with the author(s) or other rightsholder(s); author self-archiving of the accepted manuscript version of this article is solely governed by the terms of such publishing agreement and applicable law.

© The Author(s), under exclusive licence to Springer Nature Limited 2024

Methods

Materials

All chemicals were used as received unless otherwise noted. 2,2,3,3,3-Pentafluoropropyl methacrylate (PFPPMA) was purchased from SynQuest Labs. Styrene, KPS, AIBA, 75 wt% qMA aqueous solution, Pluronic F108, NaCl, THF, hexanes, ethanol, acetone- d_6 and D_2O were purchased from Sigma Aldrich. Fluorescent dyes BODIPY FL NHS ester and BODIPY 581/591 NHS ester were purchased from ThermoFisher. Adhesive microscope slide wells were purchased from Thomas Scientific and adhesive channel slides from Ibidi. Malvern Panalytical DTS1070 folded capillary cells were purchased from Fisher Scientific.

Colloidal synthesis

A common strategy to provide uniformly sized and charged polymeric colloids is through surfactant-free emulsion polymerization, whereby a charged water-soluble initiator is used such that most chains contain one charged endgroup. Generally, this has been a reliable scheme to synthesize both negative and positive colloids commonly with KPS and AIBA, respectively^{22,23}. Indeed, for well-studied monomers such as styrene or methyl methacrylate, a charged initiator is sufficient to achieve charge stability such that colloidal crystals can be assembled through the PACS method¹¹. Naively, it was thought that this approach was suitable for low-refractive-index fluorinated methacrylates as well. We found that the PFPPMA homopolymer colloids initiated with KPS retained a constant negative surface charge for years, whereas AIBA-initiated homopolymer colloids rapidly lost their positive surface charge over the course of days (Extended Data Fig. 1a–d). The progression of charge loss was surprising considering that the colloids were allowed to rest at room temperature in deionized water. We suspect that the relatively labile formamidine endgroups are much more quickly hydrolysed when near a fluorinated methacrylate relative to a styrene or methyl methacrylate due to inductive withdrawing effects^{24,25}. Rather than investigating the mechanism of formamidine degradation in the presence of fluorinated methacrylates further, we explored an alternative approach for maintaining the stability of positive charge.

We found that using a small amount of qMA comonomer afforded long-term positive charge stability. Whereas adding a positively charged comonomer is not generally new^{26–28}, we are not aware of a low refractive index (<1.4) and a stable positive charge of having been demonstrated in a colloid. Extended Data Figure 1e–h illustrates colloidal-scale quality and stability with respect to the overall monomer concentration (C_M) and fraction of qMA (C_{qMA}/C_M). Aggregation in the low-qMA regions is most probably a result of formamidine endgroup degradation due to insufficient qMA incorporation to impart long-term charge stability. Size-disperse but stable particles may be a sign of several phenomena, such as secondary nucleation of larger qMA-rich particles at later reaction times, that overlap with the growth phase of the primary nucleation pathway, or the rapid consumption of the water-soluble initiator by relatively high qMA concentrations such that the rate of termination exceeds initiation early on in the growth phase^{22,23}. The latter may be overcome by a slow continuous feed of the monomer and initiator, a strategy that may prove useful for expanding the stable size range.

For our batch conditions, where the initiator and reaction volume are held constant, SEM analysis shows a clear trend of decreasing particle diameter as the mole fraction of qMA fed is increased (Extended Data Fig. 1i,j). The inset in Extended Data Fig. 1i illustrates that, for a fixed qMA fraction, predictably, the particle size increases with PFPPMA concentration, although the effect is quite weak under the conditions tested. Furthermore, we confirmed that the size reduction is a result of the increased number of particles N_p , similar to what has been shown in cationic styrene copolymers²⁸. If the dominant nucleus-formation pathway is driven by solution-polymerized qMA-rich polymer chains, then $N_p \propto \frac{a}{a_c}$, where a is the number of qMA monomer molecules and a_c is some critical polymer size required to form a nucleus. Then we can

say that the number of particles is proportional to the qMA concentration ($N_p \approx C_{qMA}$) as long as PFPPMA is in excess and a_c remains constant between the batches. Subsequently, if we allow the reaction to reach high conversions, the volume of a particle V_p can be written simply as $V_p = \frac{V_M}{N_p}$, where V_M is the monomer volume, so the radius of the particles, R , should have a simple scaling of $R^3 \propto \frac{V_M}{C_{qMA}}$. Our size-uniform particles (blue and pink) are in good agreement with this relationship, as shown in Extended Data Fig. 1j. The break from this trend in our non-uniform batches may indicate a departure from this simple nucleation mechanism, but we note that the size variance is high and the accuracy is low for smaller particles in these batches.

Quantification of qMA copolymerized and incorporated in the colloids was determined using 1H NMR. Particles were taken directly from the synthesis, washed with water via multiple centrifugation cycles and dried at 110 °C overnight. The dried particles were dissolved in a minimal amount of acetone, and the polymers were precipitated in a $\times 50$ volume of 1:1 ethanol:hexanes, vacuum filtered and then dried again before redissolving in deuterated acetone. The incorporation appears to be linearly related to the feed with a best-fit slope of about 0.3, suggesting that 30% of the feed qMA is incorporated in the latex (Extended Data Fig. 1k,l). We recognize that the washing and precipitation procedure may extract some small-molecular-weight and qMA-rich copolymers, and that the slope may therefore underestimate the incorporation, but it is also possible that solution polymerization of qMA occurs simultaneously to consume the majority of the qMA. Overall, this approach provides effective and simple tunability in size for highly uniform low-refractive-index positively charged particles with diameters of 100–400 nm.

A typical synthetic protocol uses deionized water (100 ml), the PFPPMA monomer (8 ml), the qMA comonomer (20 μ l; 75 wt% in H_2O) and the AIBA radical initiator (0.1 g) dissolved in deionized water (5 ml) which is injected into the mixture after 1 h of nitrogen purging. All of the ingredients were mixed in a 250 ml three-neck round-bottom flask, heated to 60 °C and stirred at 330 revolutions per min under nitrogen overnight. Gravity filtration (Whatman pore size 20 μ m) was performed to remove any large aggregates; the particles were then sterically stabilized by adding 5 wt% F108 solution (1 ml) and washed via repeated sedimentation and resuspension cycles. Without the F108 surfactant, particles can still be effectively washed under low-speed centrifugation for a longer time. Negative particles were produced in the same fashion but without the comonomer, replacing AIBA with an equivalent weight amount of KPS.

Seeded growth was used to obtain colloidally stable and positively charged particles with diameters exceeding 400 nm. The same procedure as above was performed along with washed seed particles (5 ml) with a bare surface (that is, no F108 added during washing). Secondary particles with a diameter of approximately 200 nm in the supernatant were removed via low-speed centrifugation.

Fluorescent labelling of the PFPPMA systems was achieved using a swell–deswell method. To elaborate, fluorescent dye solution (100 μ l; 1 mg ml⁻¹ in toluene) dissolved in 60 vol% THF (10 ml) was added to particles stabilized with F108 to a final concentration of 30 vol% THF, then diluted by a factor of 15 and subjected to multiple sedimentation and resuspension cycles to transfer into pure water. BODIPY FL NHS ester and BODIPY 581/591 NHS ester were used for positive and negative particles, respectively.

Zeta potential

The zeta potential of particles without F108 was measured using a Malvern Zetasizer Nano ZS instrument. Particles were diluted with water to less than 0.001 wt% and equilibrated with 10 mM NaCl before being transferred into a DTS1070 folded capillary cell. Fresh samples were prepared at different time intervals to evaluate the charge stability. The zeta potential was calculated using the Smoluchowski

approximation (Henry's function $f(\kappa a) = 1.5$), using a refractive index of 1.39 for the particles.

Assembly of colloidal crystals

Binary colloidal crystals were produced via the PACS method. Oppositely charged PFPMA particles were separately equilibrated with 0.1 wt% F108 and 2–3 mM NaCl in 40% DMSO for 30 min and then mixed together while vortexing. The resulting mixture was then transferred into a glass capillary for optical microscopic observation or assembled well slides or channel slides for CLSM observation. The crystals were allowed to form overnight without disturbance. For crystallization with PS or in water, the same method was used with the different building block or medium.

CsCl-like crystals were assembled by mixing positively charged 800 nm particles and negatively charged 700 nm particles at an approximate number ratio of 1:1, whereas pure Cu₃Au-like crystals were formed by mixing positively charged 375 nm particles and negatively charged 480 nm particles at an approximate 3:1 ratio.

The optimal NaCl concentration for crystallization was dictated by the interactions described in Derjaguin–Landau–Verwey–Overbeek theory²⁹, which takes into account the solvent permittivity and radius of the particles³¹ (see ‘MD simulations’ in the Methods). Specifically, larger particles and a higher solvent permittivity (78.4 for pure water, 68 for 40% DMSO³⁰) both require a higher salt concentration for crystallization. Experimentally, a series of samples with salt concentrations ranging from 2 to 3 mM were prepared and monitored to identify the optimal conditions.

Confocal laser scanning microscopy

A z stack of scanning fluorescence images was acquired using a Leica SP8 confocal microscope equipped with a ×100 oil objective. The two BODIPY dyes were excited at 500 and 580 nm, and their emission signals were collected at 510–520 and 590–600 nm, respectively. The z-step size for the CsCl-like and Cu₃Au-like colloidal crystals was set to 0.1 and 0.07 μm, respectively. The selection of a particular z-step size was determined via the diameter of the colloidal particles used in the assembly, as conducting five to seven scans per particle is preferred for precise tracking using the Trackpy package. To prevent dye bleaching during extended scanning, we used the lowest possible laser power, typically around 5% of the maximum. We generated two-dimensional images using the Leica Application Suite X visualization software, manually rotating selected cross-sections within a reconstructed 3D structure for visualization. For each volumetric scan, defects were identified through visual inspection of the crystal planes.

The dynamics of internal defects were investigated on CsCl-like colloidal crystals, comprising positively charged 600 nm particles and negatively charged 500 nm particles, by recording time-lapse z scans with a z step of 0.08 μm and at a time interval of 30 min.

All confocal imaging, except for the images shown in Fig. 2d, was carried out in a solution of 40% DMSO.

Crystal reconstruction

The coordinates of oppositely charged particles were estimated from the greyscale images of separated channels in the z-stack data using the Trackpy Python package¹⁵. The output coordinates were imported into the Blender software and given a size based on SEM images to recreate the structure in three dimensions and to carve out particular planes or shapes.

Simulated X-ray diffraction patterns

To further identify the crystal structure, an X-ray diffraction pattern was generated using Mercury software from the particle coordinates. Initially, a certain type of binary crystal was hypothesized on the basis of the crystal planes observed via confocal microscopy. If we guessed CsCl, three neighbouring particles from experimental reconstruction

were chosen to align three specific atoms in the unit cell of CsCl. A scaling factor, translation matrix and rotation matrix were each calculated according to the position of these three atoms. The parameters were then applied to the coordinates of all of the particles. With the resulting coordinates of the reconstructed crystal and the unit-cell information of CsCl (that is, $a = b = c = 4.14369834 \text{ \AA}$ and $\alpha = \beta = \gamma = 90^\circ$), a CIF (crystallographic information file) file was generated and imported into Mercury to calculate the X-ray diffraction pattern. The X-ray diffraction pattern for a simulation result was generated via the same method.

Molecular dynamics simulations

We performed a series of coarse-grained Langevin dynamics simulations using HOOMD-blue software³¹. The attractive Coulombic interactions (V_E) between the particles were modelled using Derjaguin–Landau–Verwey–Overbeek theory²⁹, which is expressed as

$$\frac{V_E}{k_B T} = 2\pi\epsilon a\psi_+\psi_- \exp(-h/\lambda_D) \quad (1)$$

where ϵ is the solvent permittivity, which is 68 in the present work, corresponding to the 40% DMSO solution; ψ_+ and ψ_- , the surface potential values of the positive and negative particles, are set to +30 and –50 mV, respectively; h is the distance between the surfaces of the particles; λ_D is the Debye length; k_B is the Boltzmann constant; and T is the temperature. In addition, a is the effective radius arising from the Derjaguin approximation, which is expressed as $a = 2/(1/r_N + 1/r_P)$, where r_P and r_N are the radii of the positive and negative particles, respectively. Values of the repulsive potential (V_P) induced by the polymer brushes were modelled using the Alexander–de Gennes polymer brush model^{32–34} and are given by the following equation:

$$\frac{V_P}{k_B T} = \frac{16\pi r L^2 \sigma^3}{35} \left[28 \left(\left(\frac{2L}{h} \right)^{\frac{1}{4}} - 1 \right) + \frac{20}{11} \left(1 - \left(\frac{h}{2L} \right)^{\frac{11}{4}} \right) + 12 \left(\frac{h}{2L} - 1 \right) \right] \quad (2)$$

where r in the pre-factor is the repulsion radius ($r = (r_P + r_N)/2$), L is the brush length, which is 10 nm for all particles, and σ is the brush density, which is equal to 0.09 nm^{-2} .

For the CsCl size ratio, each simulation domain contained 6,750 particles, and the number ratio of positive to negative particles was 1:1. Simulations were carried out with packing fractions varying from $\phi = 0.006$ to $\phi = 0.012$ and Debye lengths from $\lambda_D = 5.45 \text{ nm}$ to $\lambda_D = 5.65 \text{ nm}$ to find the optimum conditions for obtaining a relatively large CsCl crystal with a clear rhombic dodecahedron habit (Extended Data Fig. 3).

Cu₃Au crystals did not spontaneously crystallize under the conditions tested so far; however, we found that a seed crystal placed into a box with a 3:1 ratio of positive to negative particles (13,500 in total) grew and maintained a cubic habit, confirming its stability (Extended Data Fig. 3). Visualization and analysis were performed using OVITO software³⁵.

Data availability

The data that support the findings of this study are available from the corresponding author upon request.

Code availability

Software from this work is available on GitHub at <https://github.com/hocky-research-group/CrystalClear-2024> and is archived on Zenodo at <https://doi.org/10.5281/zenodo.11126870> (ref. 36).

References

- Chern, C. Emulsion polymerization mechanisms and kinetics. *Prog. Polym. Sci.* **31**, 443–486 (2006).
- Lovell, P. A. & Schork, F. J. Fundamentals of emulsion polymerization. *Biomacromolecules* **21**, 4396–4441 (2020).

24. Shriner, R. L. & Neumann, F. W. The chemistry of the amidines. *Chem. Rev.* **35**, 351–425 (1944).
25. Fustero, S., García de la Torre, M., Pina, B. & Fuentes, A. S. New strategies for the synthesis of fluorinated vinyllogous amidines and β -enamino ketones. *J. Org. Chem.* **64**, 5551–5556 (1999).
26. Zou, H., Liu, J. & Wang, X. Surfactant-free emulsion copolymerization of styrene and a cationic comonomer with two positively charged groups. *Colloid Polym. Sci.* **297**, 1133–1142 (2019).
27. Liu, Z., Xiao, H. & Wiseman, N. Emulsifier-free emulsion copolymerization of styrene with quaternary ammonium cationic monomers. *J. Appl. Polym. Sci.* **76**, 1129–1140 (2000).
28. Meincke, T., Jordan, M., Vogel, N. & Klupp Taylor, R. N. On the size-determining role of the comonomer in the nucleation and growth of cationic polystyrene latex via emulsion polymerization. *Macromol. Chem. Phys.* **219**, 1700457 (2018).
29. Hunter, R. J. *Foundations of Colloid Science* 2nd edn (Oxford Univ. Press, 2001)
30. Lu, Z., Manias, E., Lanagan, M. & Macdonald, D. Dielectric relaxation in dimethyl sulfoxide/water mixtures. *ECS Trans.* **28**, 11 (2010).
31. Anderson, J. A., Glaser, J. & Glotzer, S. C. HOOMD-blue: a Python package for high-performance molecular dynamics and hard particle Monte Carlo simulations. *Comput. Mater. Sci.* **173**, 109363 (2020).
32. Alexander, S. Polymer adsorption on small spheres. A scaling approach. *J. Phys. Fr.* **38**, 977–981 (1977).
33. De Gennes, P.-G. Stabilité de films polymère/solvant. *C. R. Acad. Sci. II* **300**, 839–843 (1985).
34. Kleshchanok, D., Tuinier, R. & Lang, P. R. Direct measurements of polymer-induced forces. *J. Phys. Condens. Matter* **20**, 073101 (2008).
35. Stukowski, A. Visualization and analysis of atomistic simulation data with OVITO—the Open Visualization Tool. *Model. Simul. Mater. Sci. Eng.* **18**, 015012 (2009).
36. Hocky, G. hocky-research-group/CrystalClear-2024: paper reference. Zenodo <https://doi.org/10.5281/zenodo.11126870> (2024).
37. Ramasubramani, V. et al. freud: a software suite for high throughput analysis of particle simulation data. *Comput. Phys. Commun.* **254**, 107275 (2020).

Acknowledgements

This work was funded by the US Army Research Office under award number W911NF-21-1-0011. S.P. and G.M.H. were partially supported by NIH award R35GM138312. This work was supported in part through the NYU IT High Performance Computing resources, services and staff expertise, and simulations were partially executed on resources supported by the Simons Center for Computational Physical Chemistry at NYU (SF grant no. 839534). We thank M. He and C. W. Leung for assistance in the synthesis of PFPMA colloids and D. G. Grier for helpful discussion on Trackpy.

Author contributions

S.Z. designed and performed the experiments, synthesized the colloidal model systems and analysed the data. A.W.H. developed the synthesis of the positively charged fluorinated colloids, performed additional experiments and analysed the data. S.P. and G.M.H. conducted the molecular dynamics simulations and analysed the data. S.S. conceived and initiated the study. Both S.S. and G.M.H. supervised and directed the research. All authors engaged in discussing the results and analyses, contributing to the final manuscript.

Competing interests

The authors declare no competing interests.

Additional information

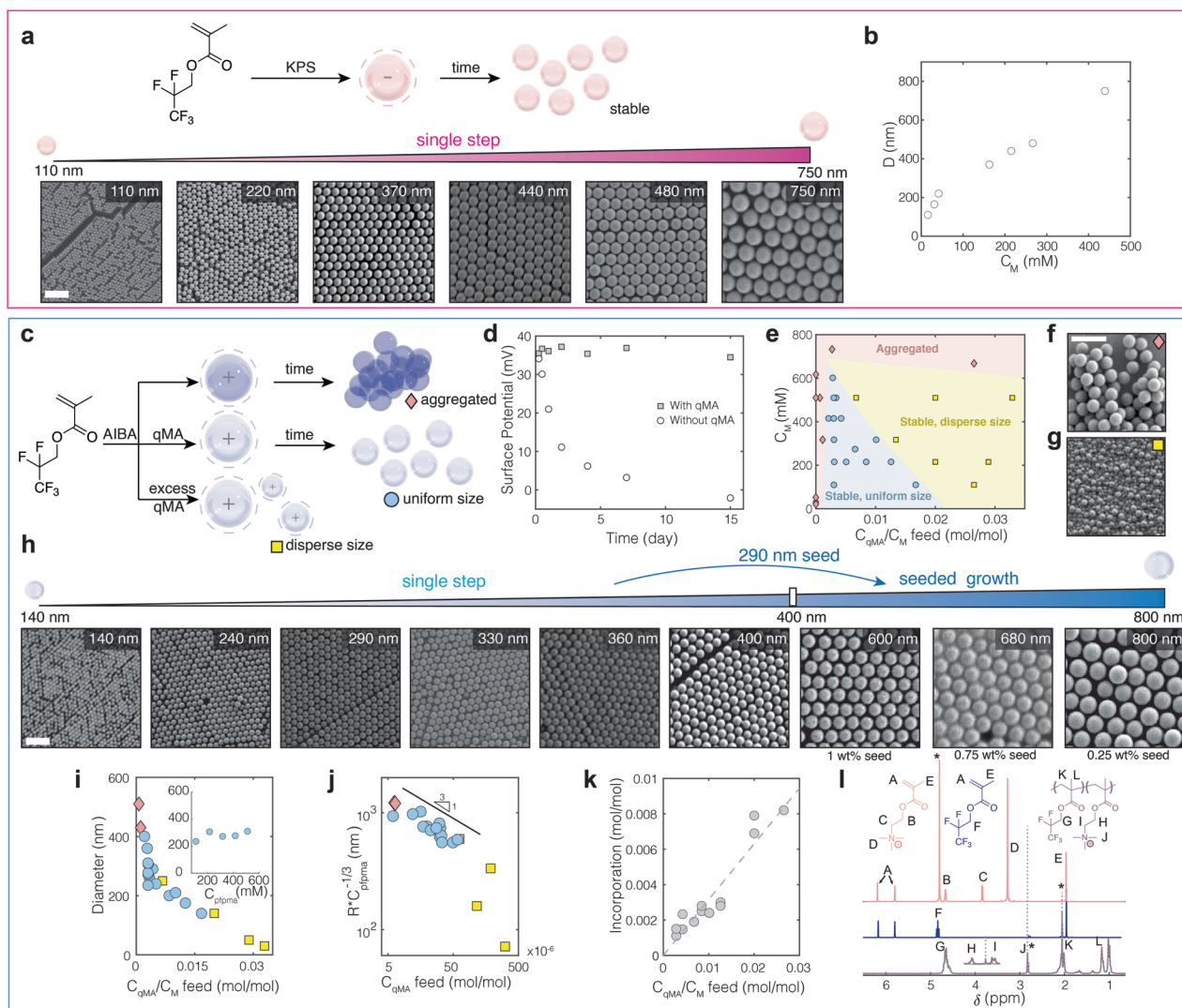
Extended data is available for this paper at <https://doi.org/10.1038/s41563-024-01917-w>.

Supplementary information The online version contains supplementary material available at <https://doi.org/10.1038/s41563-024-01917-w>.

Correspondence and requests for materials should be addressed to Glen M. Hocky or Stefano Sacanna.

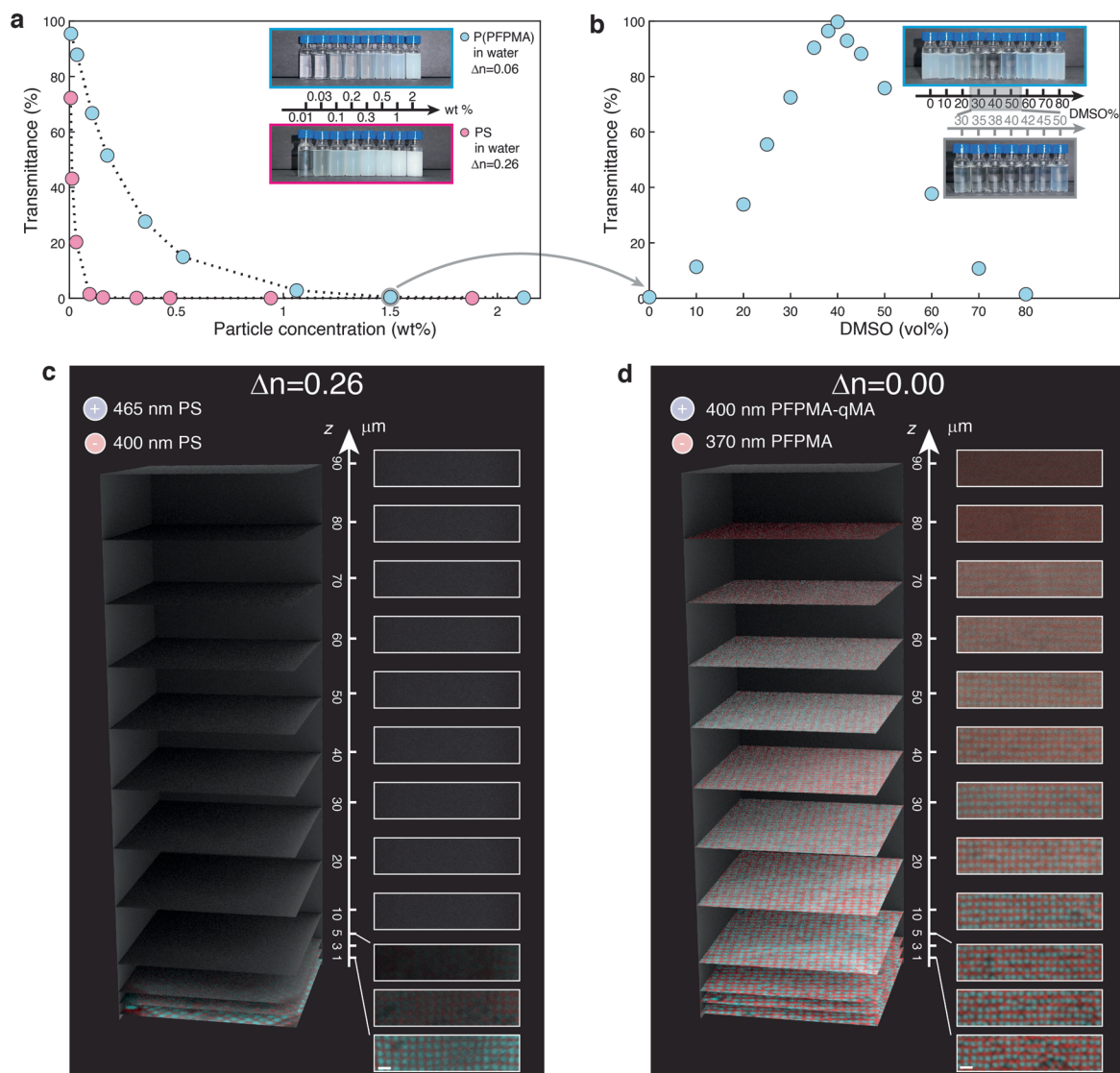
Peer review information *Nature Materials* thanks the anonymous reviewers for their contribution to the peer review of this work.

Reprints and permissions information is available at www.nature.com/reprints.



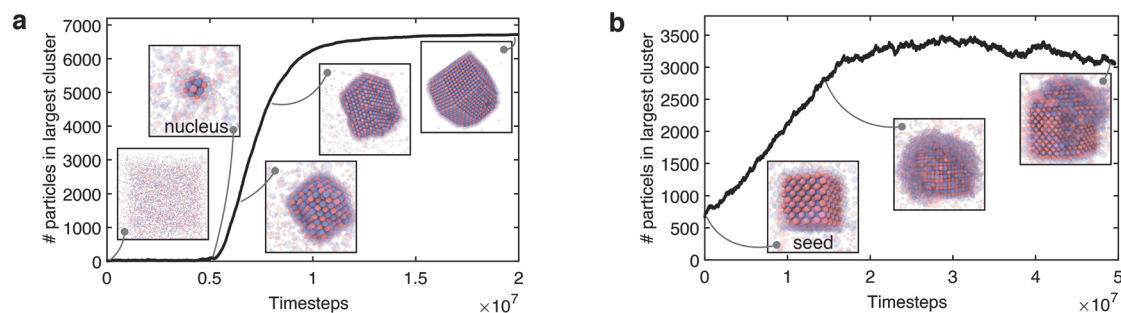
Extended Data Fig. 1 | Synthesis and characterization of oppositely charged low refractive index particles. (a) Negatively charged homopolymer particles are synthesized in batch conditions with a single-step monomer injection initiated by KPS as described in the Methods section; representative SEM images across the achievable size range are included. (b) Diameter is tuned by adjusting the monomer concentration while holding all other parameters constant. (c) Scheme to synthesize positively charged copolymer particles initiated with AIBA in batch conditions as described in the Methods section; too little or too much qMA comonomer results in aggregated or size disperse particles, respectively. (d) Time-course of measured Zeta potential for an AIBA initiated homopolymer and a stable copolymer recipe stored in deionized water shows that the former loses charge rapidly over the course of days while the copolymer remains unchanged. (e) Mole ratio qMA C_{qMA} relative to monomer C_M vs. total monomer concentration with identified regions of stable, uniform size (blue),

disperse (yellow), and aggregated (red). (f, g) SEM images of aggregated (f) and size disperse (g) particles. (h) SEM images of selected stable and uniform copolymer particles made by single step batch conditions as well as those seeded with 290 nm particles that afford particles larger than 400 nm. (i) Colloid diameter as measured by SEM plotted against relative qMA feed showing a marked decrease in size with qMA; inset shows a much weaker size relationship to monomer concentration when the qMA ratio is held constant. (j) qMA feed vs. particle radius normalized by concentration of PFPMMA to the 1/3 power showing good agreement with a qMA monomer directed nucleation in stable recipes. (k) qMA incorporation vs. feed concentration measured by ^1H NMR; best linear fit gives a slope of 0.33 suggesting that about 30% of comonomer fed remains in the colloids after purification. (l) ^1H NMR of qMA in D_2O (top) and PFPMMA (middle) monomers, poly(PFPMMA-co-qMA) (bottom, solid) and poly(PFPMMA) (bottom, broken) in acetone- d_6 . Peaks labeled with an asterisk are from solvent. Scale bars are all $1\ \mu\text{m}$.



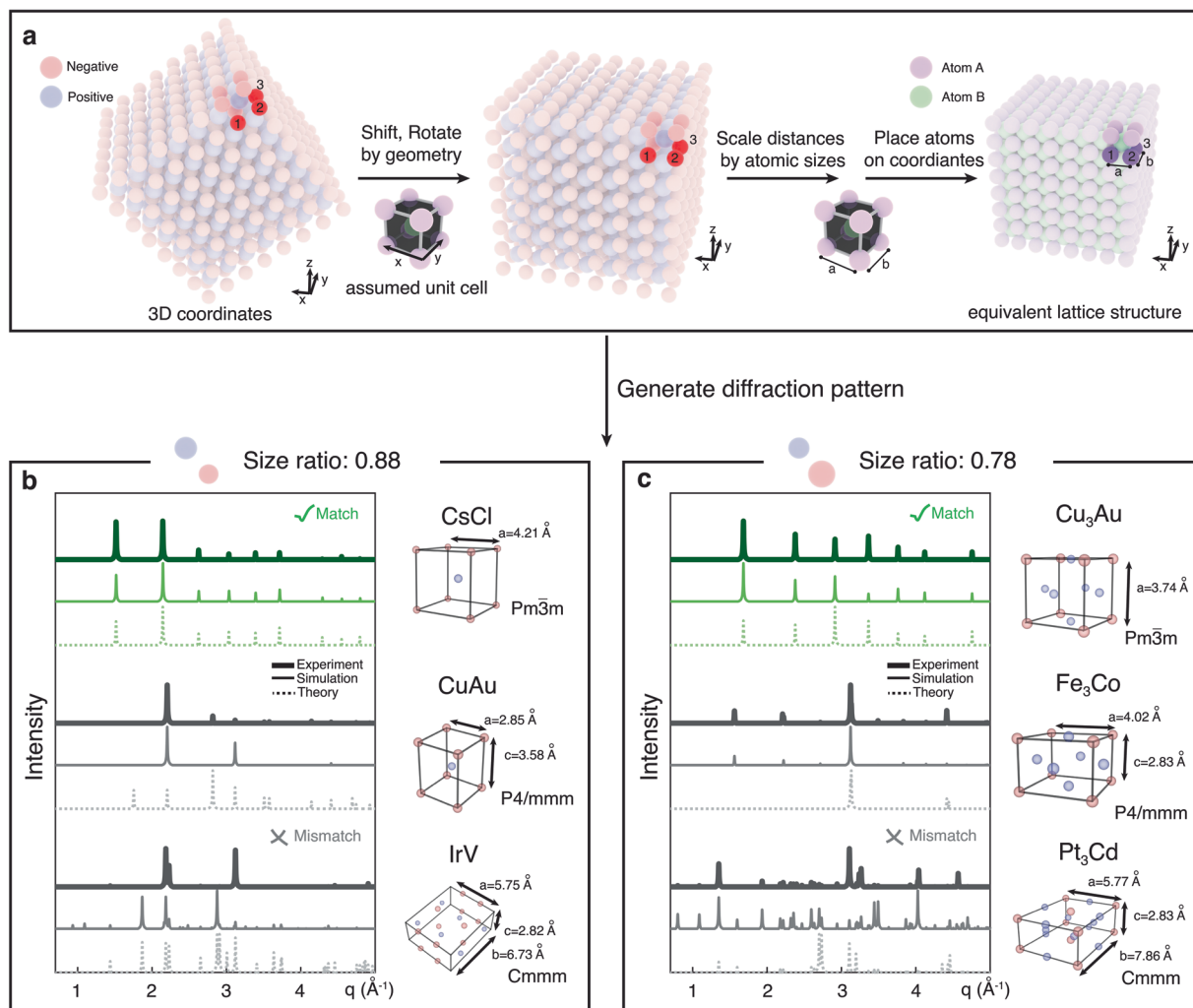
Extended Data Fig. 2 | Refractive index matching. (a) Comparative visualization and turbidity measurements of PS and PFPMA colloidal suspensions in water at varying particle concentrations. (b) To enhance the transparency of our samples, PFPMA particles were suspended in an H₂O:DMSO binary mixture. The refractive index matching point was determined by measuring transmittance against DMSO concentration for a 1.5 wt% PFPMA suspension, revealing an

optimal solvent composition of 40% DMSO. (c,d) Confocal volumetric scans were conducted on bulk crystals formed from regular PS particles in water and PFPMA particles in the matched solvent, respectively. These scans highlight the enhanced depth penetration in the PFPMA system, allowing the confocal laser to effectively probe particle positions up to a depth of ~80 μm , whereas the PS system's signal diminishes by 5 μm . Scale bars are 1 μm .



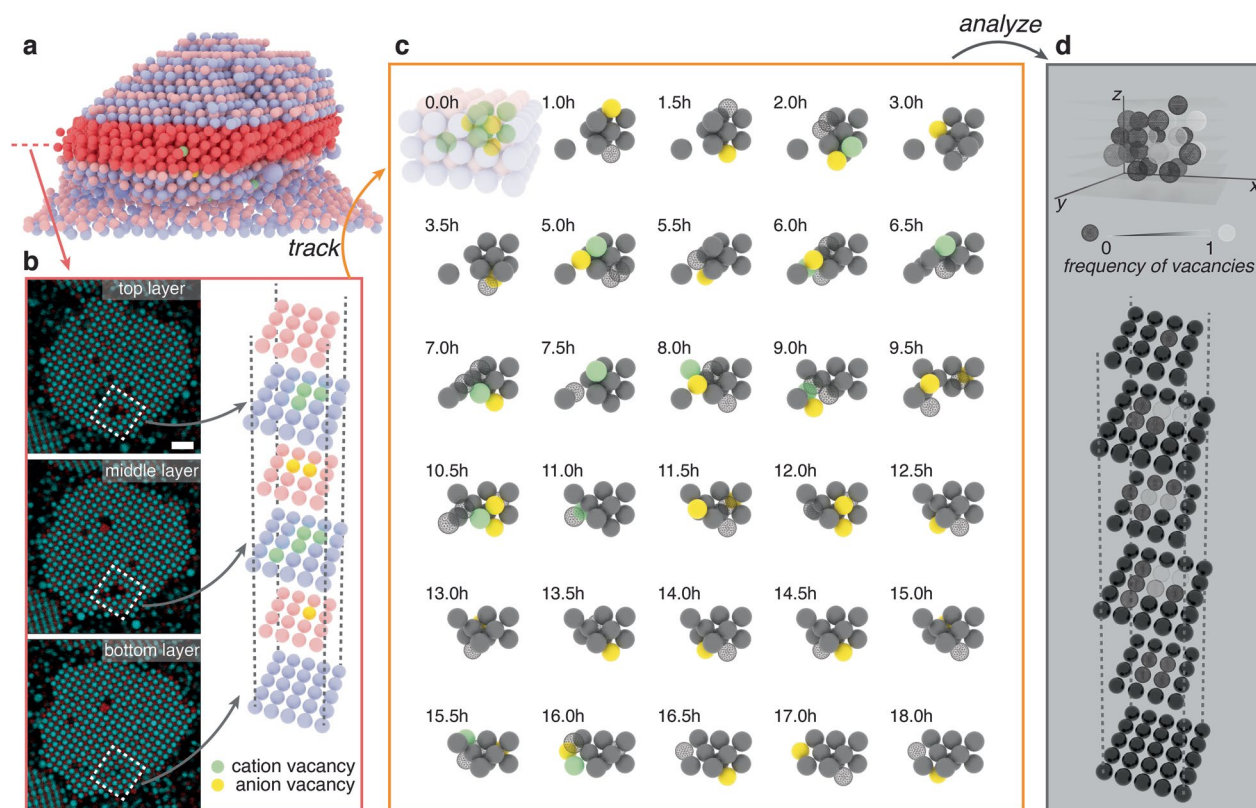
Extended Data Fig. 3 | Simulation of CsCl- and Cu₃Au-like crystals. Molecular dynamics simulations of CsCl and Cu₃Au forming systems were performed as described in Methods. Particles with crystalline environments are found using Ovito's common neighbor analysis (CNA) function³⁵ with a cutoff of 550 nm, and snapshots shown have particles with low crystallinity are set to be semi-transparent. The largest cluster size, which corresponds approximately to the size of the crystal, was computed using the Freud software³⁷ with a cutoff of 550 nm (ref. 36). **(a)** Particles of size $r_N=185$ nm and $r_P=200$ nm were simulated with Debye length $\lambda=5.5$ nm and volume fraction $\Phi=0.009$. The plot shows the resulting number of particles in the largest cluster versus time. Snapshots show representative images of the initial gas phase, a crystal nucleus, two intermediate

structures during the crystal growth, and the final structure. In the final state, almost all free particles are exhausted into a single CsCl crystal exhibiting rhombic dodecahedral habits. **(b)** A seed Cu₃Au crystal with $r_N=240$ nm and $r_P=187.5$ nm was placed in a box of those particles at volume fraction $\Phi=0.007$ and simulated with $\lambda=5.4$ nm. The seed particle had 658 total particles, with $N_P=450$ and $N_N=208$, with each edge of the cube ~ 3126 nm long. Snapshots show a magnified image of the initial seed, an intermediate, and a final state where the growth of the seed has plateaued after growing in volume by almost five times. During the growth process, the seed is coated in a disordered shell, which eventually transforms back into a structure with cubic habits.



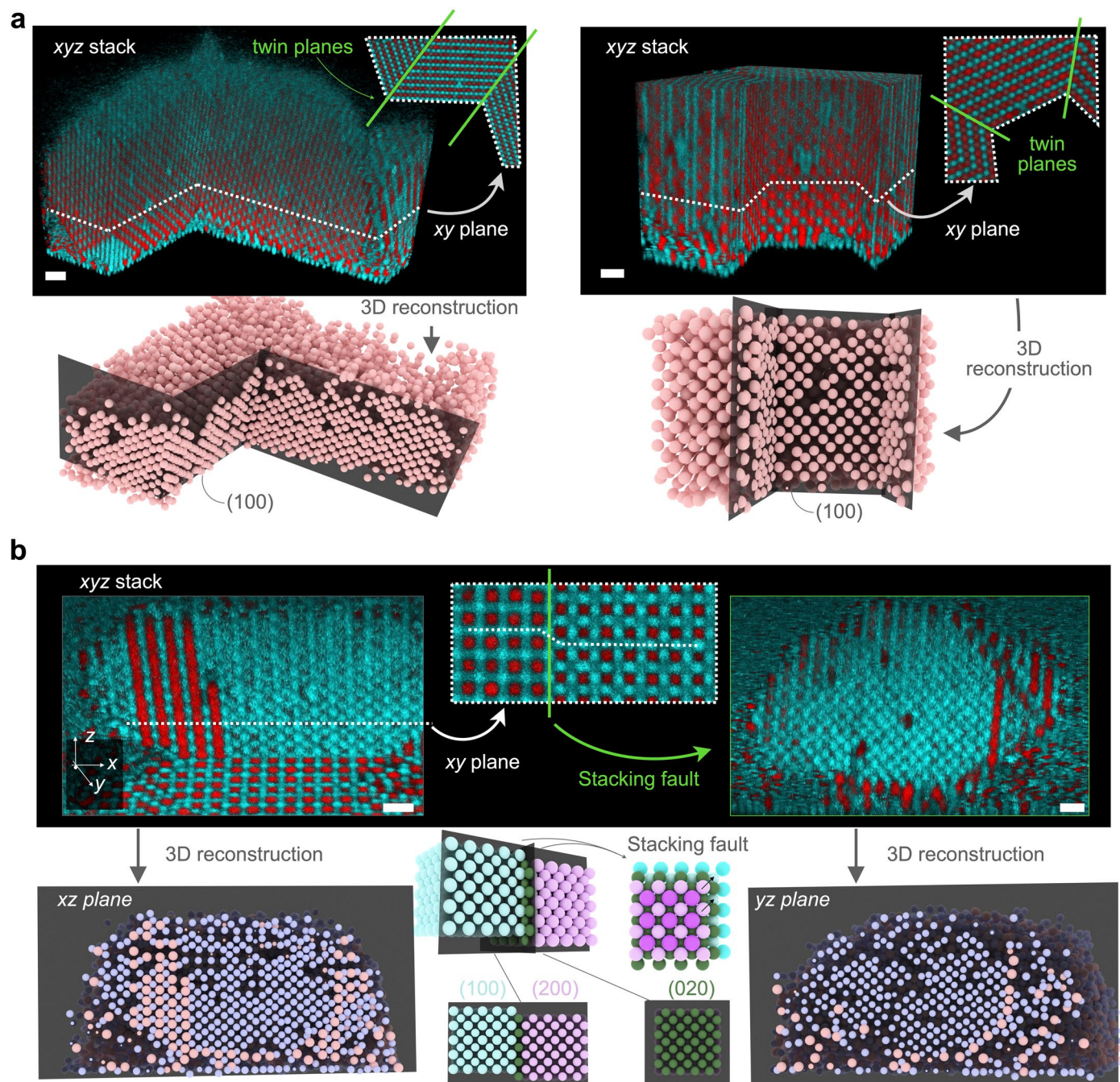
Extended Data Fig. 4 | Calculated diffraction pattern from 3D coordinates of experiments and simulation. (a) Particle coordinates, derived from experiments or simulations, are shifted, rotated, and scaled to align with a candidate lattice. These adjusted coordinates are then input into the Mercury

software to simulate the corresponding diffraction pattern. The resulting spectra can be compared with the theoretical spectra of the candidate compound. Panels (b) and (c) depict this comparison for three different candidate compounds, with crystals assembled using particle size ratios of 0.88 and 0.78, respectively.



Extended Data Fig. 5 | Defect dynamics. (a) A 3D-reconstructed snapshot capturing a CsCl crystal as it undergoes melting. Within this image, the red layers highlight the volume of interest where vacancy clusters are identified and tracked. (b) Confocal data (left) and the corresponding reconstruction (right) depict a vacancy cluster that spans three particle layers. The scale bar represents $2\ \mu\text{m}$. (c) The position of each vacancy within the volume of interest

is tracked over time, unveiling a substantial degree of particle movement. Each reconstructed frame highlights newly emerged vacancies in color, while vacancies that have disappeared are indicated by a semitransparent wire-frame. (d) Utilizing the data from particle tracking, we created a heat map that illustrates the probability of encountering a vacancy at each lattice point within the volume of interest.



Extended Data Fig. 6 | Characterization of multiple twinning and stacking faults in Cu_3Au crystals. (a) 3D confocal images alongside their reconstructed models depict Cu_3Au crystals with two consecutive twin planes, shown in parallel (left) and non-parallel (right) orientations. Digital slicing of these crystals facilitates the identification of twin boundaries, reaffirming adherence to the $\{111\}$ twin law. (b) Through similar internal analysis, we've characterized stacking

faults, a frequent 2D defect in Cu_3Au crystals. The accompanying cartoon illustrates how stacking faults arise from interruptions in the regular sequence of particle planes. The (010) planes of two crystal segments (blue and purple) are connected by a (020) plane (green) made of small particles only, which results in a plane shift along the vector $(0.5, 0, 0.5)$ (black arrows). The scale bars represent $2\ \mu\text{m}$.